CHAPTER II

THE MID-INFRARED QUANTUM CASCADE LASER

In this chapter we discuss in detail the seminal achievement by Dr. F. Capasso and his collaborators J. Faist, D. L. Sivco, C. Sirtori, A. L. Hutchinson, and A. Y. Cho of intersubband population inversion and net stimulated emission (gain) in the mid-infrared quantum cascade laser.[1,2,3]

The entire quantum-cascade-laser heterostructure, grown on a n^+-doped substrate, comprises a total of more than 500 AlInAs and GaInAs semiconductor layers. A net stimulated emission results in a set of 25 optically-active tunneling regions separated by so-called injector layers. These injector layers serve, at threshold condition (only,) as emitter and collector leads for the active tunneling regions whose working principle is as discussed in Section I.C.

The optically active 25-period superlattice of tunneling regions and interjacent injector layers is located within a waveguide core formed by surrounding cladding layers with a lower index of refraction. The variation of the index of refraction within the quantum cascade laser is designed to achieve a significant concentration of the lasing mode intensity within the optically active superlattice and thus increase the effective gain. In addition, the waveguide confinement also prevents a potential dramatic (plasmon) reabsorption in the heavily-doped top contact layers and in the InP substrate.

The lasing frequency ω_Δ is given by the mid-infrared (conduction-)subband separation $\Delta = 295$ meV between two optically active quasi-bound states of the tunneling regions. This lasing frequency corresponds to the (vacuum) wavelength, $\lambda_\Delta = 4.26\ \mu$m, that is, within one of the infrared transmission windows of the atmosphere. In addition, spontaneous intersubband emission at wavelengths, $\lambda \approx 10\ \mu$m (in the other infrared atmospheric window,) has also been reported in a modified quantum-cascade-laser design.[4]

In the original[1] (subsequent[3]) 12 $\mu\mathrm{m} \times 0.72$ mm (14 $\mu\mathrm{m} \times 1.2mm$) cleaved mesa cavity realization the mid-infrared quantum cascade laser produced a peak optical power of 8.5 (30) mW in 20 (80) ns current pulses with repetition frequency 1 (50) kHz and with a threshold heat loss $P_{th} \sim 4$ W. A recent paper[5] reports an even better performance within a slightly modified mid-infrared quantum-cascade-laser design. In addition, the seminal achievement of actual intersubband lasing[1,2,3] have fostered interest in the quantum-cascade-laser design also at QUEST, University of California, Santa Barbara, see for example Ref. 6.

The outline of this chapter is as follows. We first describe the chemical composition of the quantum-cascade-laser heterostructure[1,2,3] in general and of the optically active superlattice in particular. We explain how the digitally-graded-alloy injector layers can serve as emitter (and collector) leads for the (optically active) tunneling regions at and around the threshold conditions. Following the discussion in Section I.C we obtain a simple description of the current flow and estimate the resulting population inversion. We also discuss the threshold conditions which in particular require that the voltage drop across each superlattice period exceeds the lasing frequency, $\omega_\Delta \sim 295$ meV.

In addition we describe a theory-estimate[3] for the peak material gain, that is, the gain which would arise if the lasing mode is traveling within a (hypothetical) infinite superlattice of back-to-back tunneling regions and interjacent injector layers. We discuss the waveguide confinement which results from the variation of the index of refraction within the quantum-cascade-laser heterostructure, and explain how this confinement both increases the peak effective gain and limits the internal reabsorption. We furthermore compare threshold estimates for the effective gain with the internal loss and with the estimated rate by which the (stimulated) intersubband radiation escapes the lasing cavity.

II.A Chemical composition and tunneling potential

The quantum-cascade-laser heterostructure comprises a total of more than 500 alternating $Ga_{0.48}In_{0.52}As$ and $Al_{0.47}In_{0.53}As$ layers, grown on an InP substrate. It provides a net mid-infrared intersubband gain (at 295 meV) in just a 25-period superlattice of optically active tunneling regions and interjacent so-called injector layers. A build-in waveguide formed by layers with a low index of refraction partially confines the emitted radiation and increases the effective gain. This waveguide confinement also prevents a potentially dramatic (plasmon) reabsorption in the top heavily-doped contact layers or in the n^+-doped InP substrate.

Table 2.1, reproduced from Table 1 of Ref. 1, shows the chemical compositions on a course-grained level. Specifically, the structure comprises a central waveguide core region which includes a 25-periods superlattice (entry listed $\times\mathbf{25}$) formed by

TABLE 2.1 Overall chemical composition of the quantum-cascade-laser heterostructure formed by more than 500 alternating layers of $Ga_{0.48}In_{0.52}As$ and $Al_{0.47}In_{0.53}As$. The structure provides a net mid-infrared intersubband gain in just 25 periods of optically **active** regions with neighboring **injector** layers. Table 2.2 list the chemical composition of the active regions and Figure 2.2 shows schematics of resulting tunneling potential inside this optically active superlattice which is here represented by the single entry marked '×**25**.' The injector layers themselves comprises a multitude of layers (not listed here,) resulting in a graded effective potential designed to counter the large internal field necessary to achieve threshold conditions, see text. The optically active superlattice is located within a waveguide core with a larger effective index of refraction, $n_{mode} = 3.26$, than for the surrounding AlInAs waveguide-cladding layers described by $n_{clad} \approx 3.15$. This difference in index of refraction is increased by the inclusion in the waveguide core of two 3000 Å GaInAs layers. The variation in the index of refraction provides a partial confinement of the lasing mode within the waveguide core (see panel (a) of Figure 2.1) and thus concentrates the intensity within the optically active superlattice where the lasing mode can further stimulate the intersubband transitions. Finally, the structure includes set of top contact layers which are heavily n-doped to prevent a large contact resistance and hence a significant power dissipation by the necessary strong threshold current (listed in Table 2.3.)

TABLE 2.1

Layer type	*Material*	*Doping* [cm^{-3}]	*Thickness* [Å]	
Contact	GaInAs	2.0×10^{20}	200	
Contact	GaInAs	1.0×10^{18}	6700	
Contact	AlGaInAs Digitally graded	1.0×10^{18}	300	
Cladding	AlInAs	5.0×10^{17}	15000	
Cladding	AlInAs	1.5×10^{17}	10000	
Core	Digitally graded AlGaInAs **injector**	1.5×10^{17}	186	$\times$**1**
Core	**active** region	undoped	211	$\times$**1**
Core	GaInAs	1.0×10^{17}	3000	
Core	AlGaInAs Digitally graded	1.5×10^{17}	146	
Core	Digitally graded AlGaInAs **injector**	1.5×10^{17}	186	$\times$**25**
Core	**active** region	undoped	211	$\times$**25**
Core	GaInAs	1.0×10^{17}	3000	
Core	AlGaInAs Digitally graded	1.5×10^{17}	332	
Cladding	AlInAs	1.5×10^{17}	5000	
Cladding	n^+ doped InP Substrate			

TABLE 2.2 Chemical composition, potential, effective electron mass, and individual layer thickness of the optically **active** regions within the quantum-cascade-laser heterostructure. These triple-quantum-well resonant-tunneling regions (with effective potential shown in Figure 2.2) comprises alternating layers of AlInAs and GaInAs with effective electron masses m_e^* given in terms of the free-electron mass m_0. Note the very large conduction-band discontinuity, 520 meV, between the AlInAs and the GaInAs layers allows a triple-quantum-well potential which can confine the energetic upper resonant level E_4 in the very narrow (8 Å) first quantum-well, see Figure 2.2.

TABLE 2.2

Description:	**Active** region *Material*	*Effective potential*	m_e^*/m_0	*Layer thickness*§ [Å]
Emitter tunneling barrier	$Al_{0.48}In_{0.52}As$	520 meV	0.078	45
First (level E_4) quantum well	$Ga_{0.47}In_{0.53}As$	0 meV	0.043	8
Second tunneling barrier	$Al_{0.48}In_{0.52}As$	520 meV	0.078	35
Second quantum well	$Ga_{0.47}In_{0.53}As$	0 meV	0.043	35
Third tunneling barrier	$Al_{0.48}In_{0.52}As$	520 meV	0.078	30
Third quantum well	$Ga_{0.47}In_{0.53}As$	0 meV	0.043	28
Collector tunneling barrier	$Al_{0.48}In_{0.52}As$	520 meV	0.078	30

§ As specified in Figure 1 of Ref. 3.

optically active tunneling regions and neighboring so-called injector layer. Table 2.2 list the detailed chemical composition of the optically active triple-quantum-well tunneling regions.

The waveguide core also includes two 3000 Å GaInAs layers which serve[7] to increase the effective index of refraction, $n_{mode} = 3.26$, of the waveguide core compared with the value, $n_{clad} \approx 3.15$, for the surrounding waveguide-cladding layers of AlInAs. This variation of the index of refraction results in a partial waveguide confinement of the lasing mode which increases the effective gain, see Section II.D.

Finally the quantum-cascade-laser heterostructure includes a set of top contact layers. All of these layers are heavily n-doped to prevent a large contact resistance and thus a significant power dissipation by the necessary strong threshold current flow. The partial waveguide confinement prevent a potentially dramatic (plasmon) reabsorption in these top contact layers and in the n^+-doped InP substrate.

The bottom panel (b) of Figure 2.1 shows the *detailed* conduction-band potential of the superlattice of optically active triple-quantum-well tunneling regions (identified by the set of four thicker tunneling barriers) and the interjacent injector layers. Also shown are moduli squared of (quasi-bound) wavefunctions 2–4 (mostly contained within triple-quantum-well tunneling region) and 0–1 (extending throughout the injector layers.) The intersubband lasing results at $\omega_\Delta \approx 295$ meV from stimulated emission between quasi-bound levels 4 and 3 (formed as a combination of 3' and 3") within the tunneling regions.

We emphasize that the injector layers are themselves formed as a digital alloy, that is, by alternating AlInAs and GaInAs layers. A spacial grading of the relative thickness of the AlInAs and GaInAs layers ensures — at the threshold internal

FIGURE 2.1 [Reproduced with kind permission from Ref. 3] Detailed tunneling potential for superlattice of optically **active** regions with interjacent digital-alloy **injection** layers (panel (b)) <u>and</u> partial confinement of resulting lasing mode (panel (a).) The *bottom* panel (b) shows detailed design of both optically active regions (identified by set of four thicker tunneling barriers) *and* of digital-alloy injector layers [with voltage drop shown right to left — opposite convention used elsewhere in dissertation.] The panel (b) also shows the moduli squared of the quasi-bound wavefunctions either (mostly) confined in the ($L_{QB} = 211$ Å) active region (curves denoted 2–4) or extended throughout the ($L_{inj} = 186$ Å) injection layers (curves denoted 0 and 1.) The optical transition occurs from level 4 to level 3 (arising as a linear combination of shown wavefunction moduli squared 3' and 3".) The schematic in Figure 2.2 explains the current flow within each superlattice period. A repeated upper-subband current injection in all periods of the superlattice requires a strong internal field, $F_{dc} \sim 100$ kV/cm, so that the potential drop $eF_{dc} \times (L_{QB} + L_{Inj})$ across each superlattice period is slightly larger[3] than the optical transition frequency $\omega_\Delta \approx \Delta = E_4 - E_3 \approx 295$ meV. A fast current transport within the injector layers is nevertheless possible because the digital grading, as shown here, ensures a large density of extended states (spaghetti of wavefunction moduli squared) exactly at the shown energies *for* the threshold internal field F_{dc}. The *top* panel (a) (or insert) shows how the waveguide cladding layers provides a finite confinement of the lasing mode intensity (left axis) in the waveguide core due to the variation of the effective index of refraction (right axis.) This confinement, discussed further in Figure 2.3, concentrates a significant fraction, $\Phi \sim 0.5$, of the lasing-mode intensity within the optically active superlattice (denoted 'MQW') and thus increases the effective gain. In addition, the confinement prevents a potentially dramatic (plasmon) reabsorption in the heavily-doped top contact layers and in the substrate.

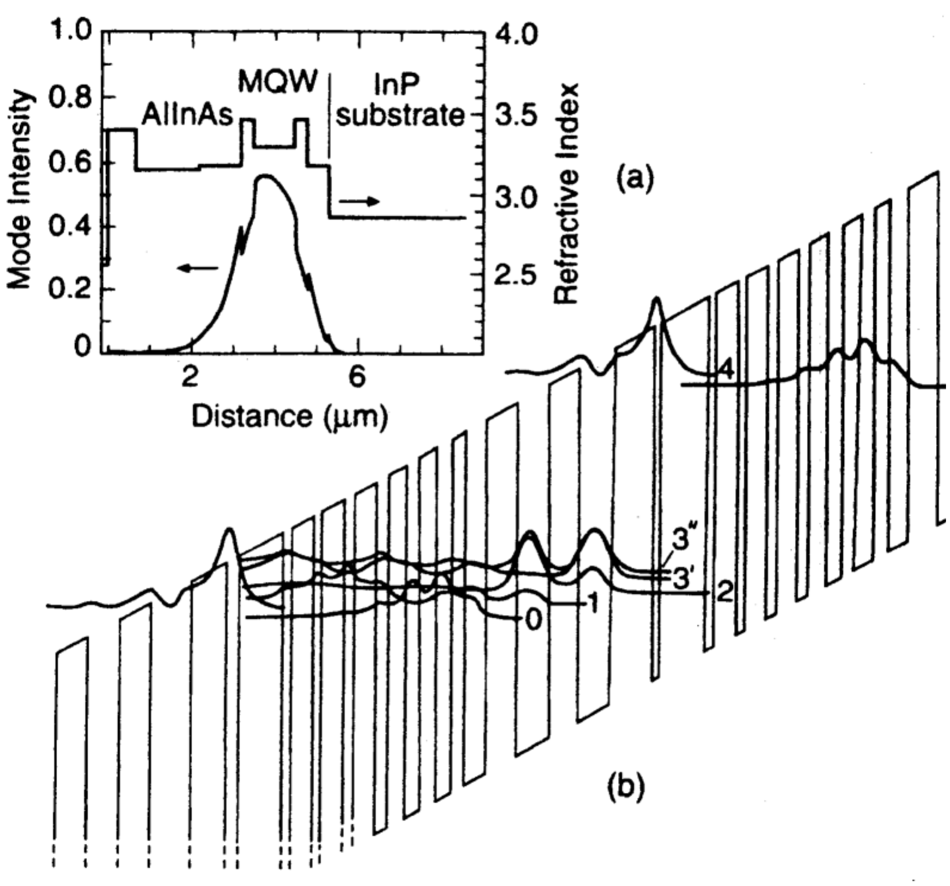
1.0
0.8
0.6
0.4
0.2
0
Mode Intensity
2
6
Distance (μm)
4.0
3.5
3.0
2.5
Refractive Index
MQW
AlInAs
InP
substrate
(a)
4
3''
3'
2
1
0
(b)

<u>**FIGURE 2.1**</u>

field $F_{dc} \sim 100$ kV/cm with illustrated resulting potential (only) — a fast electron transport between the triple-quantum-well tunneling regions. In particular, the large density of injector-layer states (spaghetti of moduli squared wavefunctions) is by design positioned exactly to allow a fast exit out from level 3 of the upstream tunneling region *and* a strong current injection into level 4 of the downstream tunneling region. In effect, the injector layers serve (at threshold conditions only) as both emitter and collector leads for the tunneling regions whose working principle is thus as described in Section I.C.

Consider finally the top panel (a) (or insert) of Figure 2.1 which illustrates how the lower (average) index of refraction (right axis) of the waveguide cladding layers ensures a partial confinement of the lasing mode (left axis) within the waveguide core. This waveguide confinement, explained schematically in Section II.D below, concentrates a significant fraction, $\Phi \sim 0.5$, of the lasing-mode intensity within the optically active superlattice (denoted 'MQW') and thus increases the effective gain. In addition, the confinement prevents a potentially dramatic (plasmon) reabsorption in the heavily-doped top contact layers and in the substrate.

II.B The threshold current flow and power dissipation

The *bottom* panel of Figure 2.2 shows schematics of the effective tunneling potential and current flow within the optically active superlattice at threshold conditions. The detailed potential within the injector layers (shown in Figure 2.1) is here in Figure 2.2 substituted by an effective potential (dotted lines) formed as the weighted average of the individual AlInAs and GaInAs layer in the digital alloy. The spacial variation of the detailed injector-layer compositions results — in

FIGURE 2.2 Schematics of threshold current flow within active tunneling regions and through injector layers (bottom panel) *realized* by build-in grading of effective injector-layer potential (dotted lines in top panel.) The detailed realization of this effective tunneling potential as a digital allow is shown in Figure 2.1. The lasing transition, indicated by wavy arrow in *bottom* panel, results between levels E_4 and E_3. The lasing threshold requires a significant internal field, $F_{dc} \sim 100$ kV/cm, to ensure a repeated current injection ($\Gamma_e \approx 3$ meV, estimated in Ref. 1) exclusively into the top optically active level 4 of subsequent active tunneling regions, see text. The digital grading of the injector layers (dotted lines in *top* panel) is designed to cancel this strong applied field and provide an almost constant effective injector-layer potential indicated by the dotted lines in *bottom* panel. The flat effective potential provides a finite density of extended states in the injector layers (as shown in Figure 2.1) which thus serves as both emitter and injector leads. The large density of extended states results in particular in a fast effective escape rate ($\Gamma_{cB} \sim 1.0$ meV, see Ref. 1) out from lower optically active level E_3 (via[1] an optical-phonon emission to level E_2.) However, only a small escape rate ($\Gamma_{cA} \sim 0.1$ meV, see again Ref. 1) results for upper level E_4.

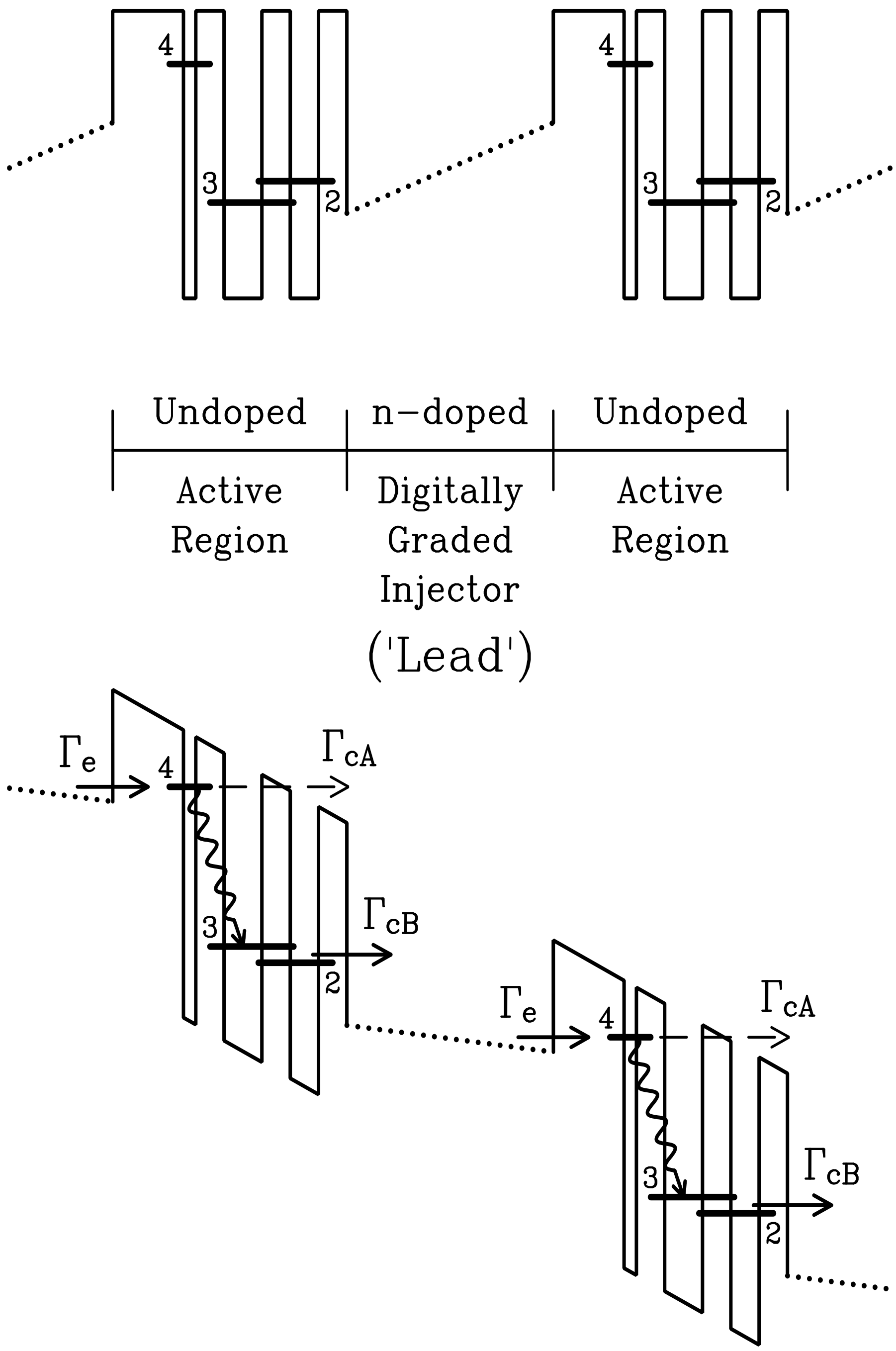
4
3
2
4
3
2
Undoped
n−doped
Undoped
Active
Region
Digitally
Graded
Injector
('Lead')
Active
Region
Γe
4
ΓcA
3
ΓcB
2
Γe
4
ΓcA
3
ΓcB
2

FIGURE 2.2

the absence of an internal field — in the graded (or sawtooth) effective potential illustrated by dotted lines in the *top* panel.

The lasing transition, indicated by wavy arrow in *bottom* panel, results between levels E_4 and E_3 with frequency $\omega_\Delta \approx \Delta \equiv E_4 - E_3$. The lasing threshold requires (a) a strong current injection Γ_e into upper level E_4, and (b) a fast (effective) lower-level escape rate Γ_{cB} out from lower optically active level E_3 *throughout* the 25 period superlattice.

An electron leaving lower level E_3 in an upstream active region [to the left of central injector layer in Figure 2.2] must in particular be able to enter to the upper-level E_4 in the downstream neighboring-period active region [to the right in Figure 2.2,] as illustrated in Figure 2.2. The lasing threshold thus requires a significant internal field, $F_{dc} \sim 100$ kV/cm, to ensure that the potential drop across one superlattice period, $(L_{QB} + L_{Inj})$, exceeds the optical transition energy, $F_{dc} \times (L_{QB} + L_{Inj}) > \omega_\Delta$, and thus allows the repeated current injection.

The digital grading of the injector layers (illustrated in the top panel) is designed to cancel this strong necessary internal field and provide an almost flat effective injector-layer potential (dotted lines in bottom panel) around the actual threshold conditions (only.) As discussed in Figure 2.1, the digital alloy provides in particular a finite density of states which extend throughout the injector layers. These states allow the injector layers to serve as emitter and collector leads and provides both a fast current injection Γ_e into level E_4 and a fast (effective) escape rate out from level E_3 (via[1] an optical-phonon emission to level E_2.) A smaller[1] escape rate Γ_{cA}, out from upper level E_4 results in part because this level must traverse two tunneling barriers to reach the injector layer. Table 2.3 list reported estimates for these tunneling rates and for the nonradiative intersubband decay rate* Γ_{nr}.

The working principle of the active regions (near threshold conditions) are as discussed in Section I.C with the injector layers serving as emitter and collector leads. We may in particular estimate the (threshold) current flow from the two-level rate equation

$$\frac{dn_A}{dt} = (N_L - n_A)\Gamma_e - n_A\Gamma_{cA} - n_A\Gamma_{nr}, \tag{1}$$
$$\frac{dn_B}{dt} = -n_B\Gamma_{cB} + n_A\Gamma_{nr}. \tag{2}$$

where the maximum upper-subband occupation density, $N_L \sim 1.5 \times 10^{11}$ cm^{-2} (as listed in Table 2.3) may be estimated as follows. Denoting the lower-band edge of the injector layer ϕ_L and assuming a quasi-Fermi level μ_L determined by the $N_{3D} = 1.5 \times 10^{17}$ cm^{-3} injector-layer doping concentration yields $\mu_L - \phi_L \sim 10$ meV. Within the quantum-well we use the low effective electron mass, $m_e^* = 0.043 m_0$, and find that the value $\mu_L - E_2 \sim 10$ meV corresponds to $N_L \sim 1.5 \times 10^{11}$ cm^{-3}.

The steady-state solution of the rate equation, Eqs. (1) and (2), yields a resulting current density

$$J = e\Gamma_e N_L \frac{\Gamma_{cA} + \Gamma_{nr}}{\Gamma_e + \Gamma_{cA} + \Gamma_{nr}}, \tag{3}$$

and population inversion

$$\Delta n = \frac{J}{e(\Gamma_{cA} + \Gamma_{nr})}\left(1 - \frac{\Gamma_{nr}}{\Gamma_{cB}}\right). \tag{4}$$

---

* This nonradiative intersubband decay is ascribed[1] to optical-phonon-emission processes. In contrast to the strong optical-phonon induced decay $E_3 \rightarrow E_2$ (which helps provides the fast effective escape rate out from quasi-bound level E_3,) the transition $E_4 \rightarrow E_3$ is not resonant with the optical-phonon frequency. The nonradiative optical-phonon induced decay $E_4 \rightarrow E_3$ is thus characterized by a large in-plane momentum transfer which ensures just a moderate value of the electron-optical-phonon interaction matrix element (given for example in Ref. 8) and a small value,[1] $\Gamma_{nr} \sim 0.15$ meV, for the estimated decay.

TABLE 2.3 Physical characteristics of the mid-infrared quantum cascade laser realized both as a 12 μm$\times$0.72 mm cleaved mesa[1] (information indicated by †) and as a 14 μm $\times$ 1.2 mm cleaved mesa[3] (information indicated by ‡.) A significant internal electric field, $F_{dc} \sim 100$ kV/cm, is required to achieve the threshold/lasing conditions with a fast current injection exclusively into upper subband E_4 of the active regions. At such internal fields the L_{inj} = 186 Å wide injector ('L') can serve as an emitter lead with quasi-Fermi sea of thickness, $\mu_L - \phi_L \sim 10$ meV given by the injector layer doping concentration $N_{3D} = 1.5 \times 10^{17}$ cm^{-3}. The resonant-tunneling current injection may thus provide a population inversion density bounded by $N_L \sim 1.5 \times 10^{11}$ cm^{-2}s, with the actual threshold population inversion being determined by the listed estimates for current injection rate Γ_e, tunneling escape rates, Γ_{cA}, and Γ_{cB}, and and nonradiative intersubband decay rate $\Gamma_{nr} \sim 0.15$ meV. The table also described the threshold current flow and large applied bias (given by the necessary strong threshold internal field F_{dc}.) The significant resulting power dissipation caused the original realizations of the quantum cascade laser to be operated in pulsed mode.[9] Finally the table also documents the increase of peak optical power which results with the longer mesa realization, Ref. 3. This increase arises in part because of the smaller cavity emission rate, α_M, see Table 2.4.

TABLE 2.3

Description:	*Symbol*	*Quantum Cascade Laser*$^{\dagger(\ddagger)}$
Configuration:$^{\dagger(\ddagger)}$ 12 μm × 0.72 mm (14 μm × 1.2 mm) mesa		
Threshold internal field$^{\dagger(\ddagger)}$	F_{dc}	~ 100 (90) kV/cm
Width of active regions	L_{QB}	$= 211$ Å
Width of injector layers	L_{Inj}	$= 186$ Å
Injector doping density	N_{3D}	$= 1.5 \times 10^{17}$ cm^{-3}
Injector Fermi sea§,‡	$\mu_L - \phi_L$	~ 10 meV
Density of tunneling states¶	N_L	$\sim 1.5 \times 10^{11}$ cm^{-2}
Emitter tunneling-in rate†	Γ_e	~ 3 meV
Upper level escape rate†	Γ_{cA}	~ 0.1 meV
Lower level escape rate†	Γ_{cB}	~ 1 meV
Nonradiative decay rate†	Γ_{nr}	~ 0.15 meV
Threshold current density$^{\dagger(\ddagger)}$	J_{th}	$= 11$ (5.35) kA/cm^2
Threshold current$^{\dagger(\ddagger)}$	I_{th}	$= 0.95$ (0.9) A
Threshold applied bias$^{\dagger(\ddagger)}$	V_{th}	$= 8$ (9.4) V
Threshold power dissipation$^{\dagger(\ddagger)}$	P_{th}	≈ 3.8 (4.2) W
Pulse duration$^{\dagger(\ddagger)}$	—	$= 20$ (80) ns
Repetition frequency$^{\dagger(\ddagger)}$	—	$= 1$ (50) kHz
Peak optical power$^{\dagger(\ddagger)}$	—	$\gtrsim 8.5$ (30) mW

$^{\dagger(\ddagger)}$ Reported in Ref. 1 (Ref. 3).

$^{\S(\P)}$ Listed (estimated) under threshold/lasing conditions.

The lasing threshold arises when the intersubband stimulated emission resulting from the population inversion, Eq. (4), exceeds both the internal loss and the rate of emission from the lasing cavity, see Section II.E.

The original two realizations were formed as a 12 μm $\times$ 0.72 mm (reported in Ref. 1) and a 14 μm $\times$ 1.2 mm (reported in Ref. 3) etched mesa with cleaved ends serving as cavity mirrors. For these structures the lasing threshold did require a very significant threshold current density, J_{th}, and also actual current flows, $I_{th} \approx 0.9$ A, as listed in Table 2.3. Because furthermore, a large threshold bias, $V_{th} \approx 8$ V, is mandated by the necessary large internal field, $F_{dc} \sim 100$ kV/cm, such large current flows results in a very significant threshold power dissipation $P_{th} \approx 4$ W. As a consequence, the first realizations of the quantum cascade laser was thus operated in the pulsed operation modes described in Table 2.4.[9]

Finally we emphasize a potential technological advantage[3,10] of the *intersubband* optical transitions in the quantum cascade laser, namely the observed small temperature-dependence of the threshold current.[3] The threshold current in standard inter-*band* semiconductor laser[11,12] exhibit a finite temperature variation.[13] This variation results in part because the spontaneous and stimulated emission involves electrons (holes) distributed within a positive-(negative-)mass conduction (valence) band and can occur at all frequencies larger than the band gab. Only a fraction of the total population inversion contributes to the actual lasing mode and this fraction *decreases* with temperature (as the electrons and holes are heated to more energetic conduction- and valence-band states respectively.) A higher temperature thus forces a larger *total* population inversion and a larger threshold current (which we assume is given by the combined nonradiative and radiative electron-hole combination rate for the total population inversion.)

In contrast, one expects a smaller threshold-current temperature dependence in the quantum-cascade-laser design because the intersubband spontaneous and stimulated emission are concentrated around just a single (lasing) frequency $\omega_\Delta \sim \Delta$. In particular, the contribution to the stimulated emission at ω_Δ from an upper-subband electron is (almost) independent of the initial in-plane momentum and is not (significantly) affected by a thermal smearing of the upper- and lower-subband electron distributions.

In practice some temperature dependence of the intersubband threshold current does result because (a) the enhanced optical emission rate reduces the population inversion, (b) the enhanced intra- and inter-subband scattering increases the line-width of the luminescence spectra and thus reduces the peak gain (see Section II.C) and because (c) the tunneling escape rate out from the lower optically active level decreases with temperature since some of the final collector states becomes occupied.[3] Nevertheless, the threshold-current temperature dependence of the *intersubband* quantum cascade laser remains small at $T \lesssim 100$ K, as shown in the top insert of Figure 3 in Ref. 3.

II.C The peak material gain

The material gain is defined as the stimulated emission rate for the lasing mode if traveling *exclusively* within a superlattice of optically active tunneling regions and the interjacent injector layers (both described in Section II.A.) We report here a simple estimate of the *peak* material gain, γ_{mat}, based on a theoretical[3] determination of the total spontaneous emission. Our discussion follows essentially the treatment in Ref. 14.

To estimate the material gain we consider a fictitious material made up entirely of back-to-back active-region/injector-layer periods. We assume for this material a homogeneous dielectric constant, $\epsilon_r = n_r^2$, and describe the electromagnetic field by the (quantized) vector potential

$$\vec{A}(\vec{r},t) = \sum_{\vec{q},\eta} \left(\frac{2\pi c^2}{L^3 \omega_{\vec{q}} \epsilon_r} \right)^{1/2} \vec{\xi}(\vec{q},\eta) \times \exp(i\vec{q}\cdot\vec{r}) \left[a_{\vec{q},\eta} e^{-i\omega_{\vec{q}} t} + \text{h.c.} \right], \tag{5}$$

where $\vec{\xi}(\vec{q},\eta)$ denotes the polarization of the cavity mode $(\vec{q},\eta)$. We consider a bulk 'cavity' of volume L^3 where the spacial dimension is L much larger than the wavelength $\lambda_\Delta \sim 4$ mu of the lasing mode. We also assume Transverse-Electro-Magnetic (TEM) modes with polarization perpendicular to the direction of propagation.

The optical transition between an initial upper-subband state, $|\Psi_4, \vec{k}_i\rangle$, and a final lower subband state, $|\Psi_3, \vec{k}_f\rangle$, is described by dipole matrix element

$$\langle \Psi_4, \vec{k}_i | (y,z) | \Psi_3, \vec{k}_f \rangle \propto \langle \Psi_4 | \Psi_3 \rangle \equiv 0, \tag{6}$$

and

$$\begin{aligned} \langle \Psi_4, \vec{k}_i | x | \Psi_3, \vec{k}_f \rangle &= \delta_{\vec{k}_i,\vec{k}_f} \langle \Psi_4 | x | \Psi_3 \rangle \\ &= \delta_{\vec{k}_i,\vec{k}_f} \int dx \Psi_4(x)\, x\, \Psi_3(x). \end{aligned} \tag{7}$$

where we have ignored the optical in-plane momentum transfer. Within this simplified description it is thus, for a given radiation mode $(\vec{q},\eta)$, only the $\hat{x}$-component (parallel to the current flow) of the electric field

$$E(\vec{r},t) = -\frac{1}{c}\frac{\partial A_x}{\partial t} \propto \xi_x(\vec{q},\eta), \tag{8}$$

which causes the intersubband transition.

On the other hand, a cavity mode $(\vec{q},\eta)$ polarized in the $\hat{x}$-direction (i.e., with $\xi_x(\vec{q},\eta)=1$) does result in the very significant interaction

$$H_{\vec{q},\eta}(t) = e\,x\;i\sum_{\vec{q},\eta}\left(\frac{2\pi\omega_{\vec{q}}}{L^3\omega_{\vec{q}\epsilon_r}}\right)^{1/2}\xi_x(\vec{q},\eta)\left[a_{\vec{q},\eta}\exp(-i\omega_{\vec{q}}t)+\text{h.c.}\right]. \tag{9}$$

In particular, the dipole matrix element characterizing this interaction, Eq. (9), is estimated[3] at $\langle\Psi_4|x|\Psi_3\rangle \approx 10$ Å corresponding to a very significant oscillator strength

$$f_{43} = 2m_e^*(E_4-E_3)|\langle\Psi_4|x|\Psi_3\rangle|^2 \approx 0.4. \tag{10}$$

Such large (resonant) values of the oscillator strength result because the quantum-confinement concentrates the total oscillator strength on just a few possible optical transitions — an important build-in advantage of *intersubband* optical transitions which is thus exploited in the quantum-cascade-laser design.

For a *single* electromagnetic mode $(\vec{q},\eta)$ of energy $\omega_{\vec{q}} = |\vec{q}|c/n_r$ and containing $n_{\vec{q},\eta}$ photons we next evaluate the transition rate between occupied upper-subband initial state $(\Psi_4,\vec{k}_i)$ and empty lower-subband final state $(\Psi_3,\vec{k}_f)$. Using the Fermi golden rule we find

$$\Gamma_{(4\vec{k}_i)\to(3\vec{k}_f)}(n_{\vec{q},\eta}) = 2\pi\left|\langle\Psi_4,n_{\vec{q},\eta}|H_{\vec{q},\eta}(t)|\Psi_3,n_{\vec{q}\eta}+1\rangle\right|^2\delta_{\vec{k}_i,\vec{k}_f}\,\delta(\Delta-\omega_{\vec{q}}) \tag{11}$$

Note that within the above simple treatment the optical transition rate is *independent* of $\vec{k}_i=\vec{k}_f$, and in particular independent of any thermal smearing of the upper-subband initial distribution. This observation helps account for the observed[3] small temperature dependence of the threshold current — an potentially technological advantage[10] briefly discussed in Section II.B.

For every pair, $(|\Psi_4,\vec{k}\rangle,|\Psi_3,\vec{k}\rangle)$, of an occupied upper-subband initial state with a corresponding empty lower-subband final state, we obtain the intersubband transition rate Eq. (11) as a sum

$$\Gamma_{4\to 3}(\vec{q},\eta) = \Gamma_{43}^{sp}(\vec{q},\eta) + \Gamma_{43}^{st}(\vec{q},\eta), \tag{12}$$

$$\Gamma_{43}^{sp}(\vec{q},\eta) = \left(\frac{e^2}{\epsilon_r}\right) |\langle\Psi_4|x|\Psi_3\rangle|^2 \frac{(2\pi)^2}{L^3} |\xi_x(\vec{q},\eta)|^2 \omega_{\vec{q}}\delta(\Delta - \omega_{\vec{q}}), \tag{13}$$

$$\Gamma_{43}^{st}(n_{\vec{q},\eta}) = n_{\vec{q},\eta}\Gamma_{43}^{sp}(\vec{q},\eta), \tag{14}$$

of a spontaneous ($\Gamma_{43}^{sp}(\vec{q},\eta)$) and a stimulated ($\Gamma_{43}^{st}(\vec{q},\eta)$) emission rate. Using the standard result,

$$\sum_{\eta} \int d\Omega_{\vec{q}} \xi_x(\vec{q},\eta)^2 = \frac{8\pi}{3}, \tag{15}$$

we sum Eq. (13) over all modes inside our L^3 cavity and thus estimate the *integrated* spontaneous emission rate

$$\begin{aligned} \Gamma_{43}^{sp} &= \sum_{\vec{q},\eta} \Gamma_{43}^{sp}(\vec{q},\eta) \\ &= \frac{4}{3}\left(\frac{e^2}{\epsilon_r}\right)\left(\frac{n_r}{c}\right)^3 \Delta^3 |\langle\Psi_4|x|\Psi_3\rangle|^2, \\ &= \frac{1}{3} n_r \alpha^3 \left(\frac{|\langle\Psi_4|x|\Psi_3\rangle|}{a_0}\right)^2 \Delta^3/\mathrm{Ry}^2, \end{aligned} \tag{16}$$

expressed in terms of the fine-structure constant α, and the (unscaled) Bohr radius and Rydberg, a_0, Ry.

In a simple theoretical estimate of the integrated spontaneous emission rate for the mid-infrared quantum cascade laser we use $\Delta = 295$ meV, $\langle\Psi_4|x|\Psi_3\rangle = 10$ Å, and take for the assumed homogeneous index of refraction n_r the value, $n_r = n_{mode} = 3.26$, that is, the estimated[3] *effective* (or average) index of refraction for the lasing mode. Inserting these numbers we find

$$\Gamma_{43}^{sp} \equiv \frac{1}{\tau_{sp}} \approx 3 \times 10^{-5} \text{ meV}. \tag{17}$$

corresponding to the small spontaneous decay time $\tau_{sp} \approx 14$ ns. This estimate is in good agreement with the value $\tau_R = 13$ ns reported in Ref. 1.

The above results Eqs. (13), (14), and (16) assume that there is only one possible transition energy, namely the subband separation Δ. However, the actual luminescence (i.e., the spontaneous emission) is observed within a distribution of energies,

$$\Gamma_{43}^{sp}(\omega) \equiv \Gamma_{43}^{sp} \times \frac{a(\omega)}{2\pi}, \tag{18}$$

described by a line-shape function $a(\omega)/2\pi$ normalized to unity. Figure 4 of Ref. 3 shows this line-shape function (see the low-current curve) which is of course still strongly peaked at a frequency ω_Δ given by the subband separation Δ. For the quantum cascade laser one can assume[3] a Lorentzian form

$$a(\omega) = \frac{2\Gamma_\phi}{(\omega - \omega_\Delta)^2 + \Gamma_\phi^2}. \tag{19}$$

of with a $2\Gamma_\phi = 22$ meV full-width-half-maximum value at $T = 10$ K, see Ref. [3].

Following Ref. 14 we account for this line-shape of the spontaneous emission rate, Eq. (18), by assuming that $a(\Delta')/2\pi$, describes the *distribution* of energy differences in the optically active pairs comprising the occupied initial upper-subband state and corresponding empty final lower-subband state. Such a distribution of transition energies arises because (a) the inter- and intra-subband scattering leads to a broadening of both the initial and final subband states, (b) the optical momentum transfer is not exactly zero causing the optical transition energy (Δ) to depend on the initial electron in-plane momentum even when assuming parallel parabolic subbands, and finally because (c) the assumption of such parabolic subbands is only approximate.[1] The large line-width observed in the quantum cascade laser is in Ref. 3 ascribed primarily to the strong interface scattering in the narrow 8 Å quantum well containing the most energetic level 4.

Rather than Eqs. (13) and (14), the intersubband spontaneous and stimulated emission into mode $(\vec{q}, \eta)$ may thus be approximated by the *averaged* rates

$$\overline{\Gamma}^{sp}_{43}(\vec{q}, \eta) = \frac{\omega_{\vec{q}}}{L^3} \left(\frac{e^2}{\epsilon_r} \right) |\langle \Psi_4 | x | \Psi_3 \rangle|^2 2\pi a(\omega_{\vec{q}}), \tag{20}$$

$$\overline{\Gamma}^{st}_{43}(\vec{q}, \eta) = n_{\vec{q},\eta} \overline{\Gamma}^{sp}_{43}(\vec{q}, \eta), \tag{21}$$

arising by integrating Eqs. (13) and (14), respectively, over the assumed distribution of the parameter Δ'. We note that summing Eq. (20) over all modes of frequency ω reproduces the experimentally observed result Eq. (18).

Using the above described heuristic approach we find for the lasing mode polarized in the $\hat{x}$-direction and having n_Δ photons of frequency ω_Δ, a stimulated emission rate

$$\overline{\Gamma}^{st}_{43}(n_\Delta) = W_{3D}(n_\Delta) \Gamma^{sp}_{43} \left(\frac{3\pi c^3}{2 n_r^3 \omega_\Delta^3} \right) a(\omega_\Delta). \tag{22}$$

This rate is directly proportional to the total integrated spontaneous emission rate Γ^{sp}_{43} estimated above and to the energy density

$$W_{3D}(\omega_\Delta) = \frac{n_\Delta \omega_\Delta}{L^3}, \tag{23}$$

of the lasing mode inside the L^3 cavity.

To provide a simple estimate of the peak material gain γ_{mat} we consider the propagation of the lasing mode in the in-plane direction (perpendicular to the current flow.) We denote by $\hat{y}$ the direction of this in-plane propagation and assume the following spacial variation

$$E(y, t) = \frac{1}{2} \left[E_0 e^{i(q_\Delta y - \omega_\Delta)} + \text{c.c.} \right] \exp\left(\gamma_{mat}(\omega_\Delta) y/2 \right), \tag{24}$$

$$W_{3D}(y,\omega_\Delta) = \frac{1}{8\pi}\epsilon_r|E_0|^2 \exp\left(\gamma_{mat}(\omega_\Delta)y\right), \tag{25}$$

$$S(y,\omega_\Delta) = \frac{c}{n_r}W_{3D}(y,\omega_\Delta) = \frac{c}{8\pi}n_r|E_0|^2 \exp\left(\gamma_{mat}(\omega_\Delta)y\right), \tag{25}$$

for the lasing mode electric field, energy density and radiation intensity, respectively. The amplification of the radiation intensity

$$\frac{dS(y,\omega_\Delta)}{dy} = \gamma_{mat}(\omega_\Delta)S(y,\omega_\Delta) \tag{26}$$

is just the lasing frequency ω_Δ *times* the net number of emission processes (i.e., emission minus absorption) produced within a unit volume containing $1/(L_{QB} + L_{Inj})$ periods and having the total population inversion

$$\Delta n_{(3D)} = \frac{\Delta n}{L_{QB} + L_{Inj}}. \tag{27}$$

The resulting material gain,

$$\begin{aligned}\gamma_{mat}(\omega_\Delta) &= \Delta n_{(3D)}\Gamma_{43}^{st}(\omega_\Delta)\omega_\Delta/S(y,\omega_\Delta)\\ &\approx \left(\frac{3\pi c^2}{2n_r^2\omega_\Delta^2}\right)\frac{\Delta n}{(L_{QB}+L_{Inj})}\Gamma_{43}^{sp}a(\omega_\Delta),\end{aligned} \tag{28}$$

is proportional to the intersubband population inversion density Δn and, assuming a constant nonradiative decay rate Γ_{nr}, proportional to the current density J, see (4). Following Refs. 1 and 3 we can thus introduce the so-called normalized gain coefficient

$$\gamma_{mat} \equiv gJ, \tag{29}$$

for which we above have derived the theoretically estimated

$$g \approx \left(1 - \frac{\Gamma_{nr}}{\Gamma_{cB}}\right)\frac{3\pi c^2\Gamma_{43}^{sp}\, a(\omega_\Delta)}{2n_r^2\omega_\Delta^2(L_{QB}+L_{Inj})e(\Gamma_{cB}+\Gamma_{nr})}. \tag{30}$$

Assuming $\Gamma_{nr} \ll \Gamma_{cB}$ (valid for the mid-infrared quantum cascade laser) and using Eq. (16) to estimate Γ_{43}^{sp}, the above expression Eq. (29) is identical to the theory estimate provided in Ref. 3. The reported numerical value of this theory-estimate is[3] $g \approx 29$ cm/kA. For comparison we note that Ref. 1 reports the estimate $g \approx 9$ cm/kA based on an experimental measurement of the total integrated luminescence Γ_{43}^{sp} at the lasing threshold. Both values are reported in Table 2.4.

Finally, we emphasize that the peak stimulated emission, the peak material gain, and hence the normalized gain coefficient is all proportional to the peak value $a(\omega_\Delta) = 2/\Gamma_\phi$, of the line-shape function. That is, the peak gain is *inversely* proportional to the full-width-half-maximum line-width $2\Gamma_\phi$. In the original quantum-cascade-laser design discussed above this broadening was large primarily because the optical active transition originates in the very narrow first quantum well (see Figure 2.2) and thus very sensitive to interface scattering, see Ref. 3. We note in particular that an significant improvement of the peak material gain was achieved in a modified design[5] in which the optical transitions occurs between two levels of a wider quantum wells and that this improvement can be explained[10] by the expected reduced interface scattering.*

II.D The waveguide confinement

The discussion in the previous section addressed only the material γ_{mat}, that is, the gain in a hypothetical infinite superlattice comprising back-to-back active-region/injector-layer periods. However, the vacuum wavelength of the lasing mode

* One can hope that the material gain in the hypothetical *far-infrared* quantum-cascade-laser design introduced in Chapter I also will benefit from a narrower line-width because the optical transitions results between quasi-bound levels in relative wide quantum wells. We note in particular that the experimentally observed absorption line-width in the corresponding isolated quantum-well structure investigated in Refs. 15, 16 is $2\Gamma_\phi \lesssim 1$ meV at low temperatures, $T \sim 10$ K.

is $\lambda_\Delta = 4.2$ μm which inside the waveguide core (with effective index of refraction $n_{mode} = 3.26$) corresponds to the modified wavelength, $\lambda_\Delta / n_{mode} \approx 1.3$ μm. This modified wavelength is, however, comparable to the total extension of the 25-period superlattice, $25 \times (L_{QB} + L_{Inj}) \approx 1$ μm and the estimated material gain must be adjusted to predict the *effective* (actual) gain arising within the optically active, but finite, superlattice.

Following the treatment in Ref. 17 one can estimate the resulting (reduced) *effective* gain γ_{mat} (defined as the actual gain resulting from the 25-period superlattice of the quantum-cascade-laser heterostructure) simply by weighting the peak material gain by the fraction Φ of the lasing-mode intensity actually inside the finite superlattice,

$$\gamma_{eff} \approx \Phi \gamma_{mat}. \tag{31}$$

The design of a good waveguide, allowing a significant value of this so-called waveguide-confinement factor Φ, is thus an important part of the quantum-cascade-laser heterostructure. This is particularly so because a large value of Φ not only increases the effective gain, Eq. (31), but at the same time also limits the reabsorption α_I in the regions outside the waveguide core as discussed in Section II.E. A detailed account for the large value $\Phi \approx 0.46$ reported in Ref. 1 is beyond the present scope but we include below a simple discussion.

Consider the radiation field for the lasing mode

$$E(\vec{R};t) = \left[E_{ac}(\vec{R}) \exp\left(-i\omega_\Delta t\right) + \mathrm{c.c} \right], \tag{32}$$

which we (thanks to the waveguide cladding layers) shall assume propagates entirely in the in-plane direction $\hat{y}$, see Figure 2.3. We also assume for simplicity that the

FIGURE 2.3 Waveguide confinement of mid-infrared lasing mode q_{rad} *explained* by variation in effective index of refraction. The *top* panel shows the lasing mode which we assume polarized in the tunneling/growth direction ($\hat{x}$) perpendicular to the waveguide plane and propagating in the in-plane $\hat{y}$-direction indicated by wavevector q_{rad}. The middle and lower panels show the variation of effective index of refraction $n_r(x)$ within the quantum-cascade-laser heterostructure and resulting waveguide confinement potential, $\phi_\omega(x) = -n_r(x)^2(\omega^2/c^2)$, which enters into an approximate HelmHoltz equation for the lasing-mode radiation field E_{ac}, see text. As indicated by the dotted line in the *middle* panel, we assume for the waveguide core a constant index of refraction, $n_{mode} = 3.26$, estimated[3] as the *effective* index of refraction for the lasing mode $q_{rad} = n_{mode}(\omega_\Delta/c)$. The middle panel also illustrate how the inclusion of two 3000 Å GaInAs layers, with large index of refraction $n_r > 3.4$, increases[7] this effective waveguide-core index of refraction, $n_{mode} = 3.26$, compared with the index of refraction, $n_{clad} \approx 3.15$, of the surrounding waveguide-cladding layers. For the approximate waveguide confinement potential, shown in the *bottom* panel, the larger difference, $n^2_{mode} - n^2_{clad}$, implies a deeper potential and a shorter decay length, $1/\kappa \sim c/(\omega_\Delta\sqrt{n^2_{mode} - n^2_{clad}}) \approx 0.4\ \mu$m, of the lasing mode into the cladding layers.

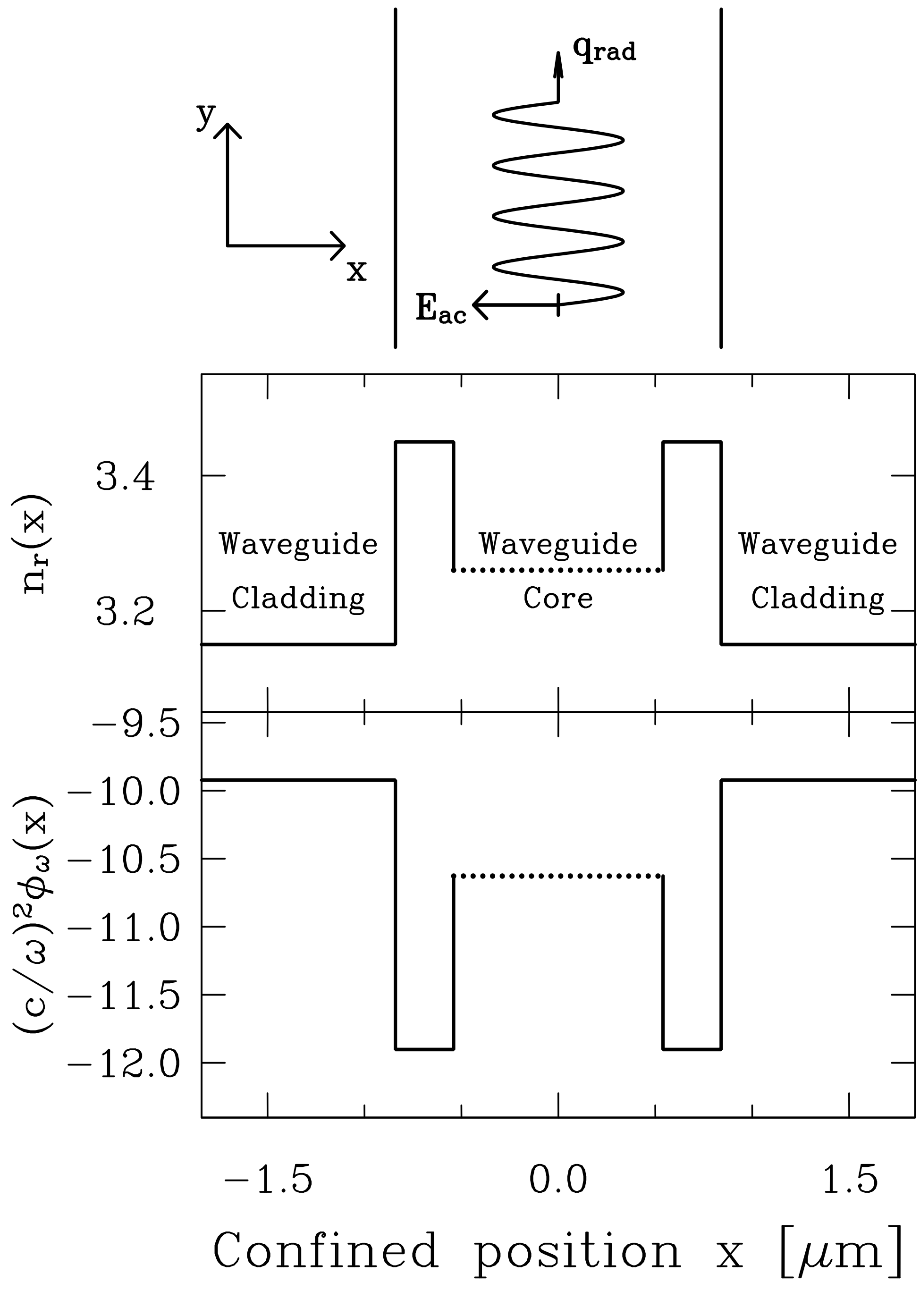

q_{rad}
y
x
E_{ac}
3.4
3.2
$n_r(x)$
Waveguide
Cladding
Waveguide
Core
Waveguide
Cladding
−9.5
−10.0
−10.5
−11.0
−11.5
−12.0
$(c/\omega)^2\phi_\omega(x)$
−1.5
0.0
1.5
Confined position x [μm]

FIGURE 2.3

radiation constitute a TE-mode[18] and is polarized entirely in the growth direction $\hat{x}$ (as indicated in Figure 2.3.) The x-component of the electric field can be written

$$E_{ac}(\vec{R}) = E_0(x,z)e^{iq_{rad}(x)y}. \tag{33}$$

Here the radiation wavevector,

$$q_{rad}(x) \equiv n_r(x)\frac{2\pi}{\lambda_\Delta}, \tag{34}$$

is given by the vacuum wavelength λ_Δ of the lasing mode but assumed modified by the index of refraction $n_r(x)$ for the specific heterostructure layer at position x. However, for the waveguide-guide region we shall assume just a constant index of refraction, $n_{mode} = 3.26$, given as the estimated[3,7] effective value for the lasing mode, $q_{rad} = n_{mode}(\omega_\Delta/c)$.

The spacial (x) variation of the index of refraction $n_r(x)$ results in a corresponding variation of the background dielectric constant $\epsilon_r(x) \equiv n_r(x)^2$. In addition there is also a plasmon contribution to the dielectric constant arising from the finite conductivity $\sigma(x)$ of the heterostructure layer at position x. Within a simple Drude description we have

$$\sigma(x;\omega) = \frac{\sigma_0(x)}{1 - i\omega\tau}, \tag{35}$$

$$\sigma_0(x) = N_{3D}(x)\,\frac{e^2/\epsilon_0(x)}{m_e^*(x)}, \tag{36}$$

where m_e^* ($N_{3D}(x)$) represents the local effective mass (carrier concentration) and $1/\tau \sim 1$ meV denotes the relaxation rate. The local plasmon frequency

$$\begin{aligned}\Omega_{pl}(x) &= \left(\frac{4\pi N_{3D}(x)e^2}{\epsilon_0(x)m_e^*}\right)^{1/2} \\ &= 4\mathrm{Ry}^*(x)\sqrt{N_{3D}(x)\pi a_*^3}\end{aligned} \tag{37}$$

expressed in terms of the local scaled Rydberg, $\mathrm{Ry}^*(x)$, and scaled Bohr radius, $a_*(x)$, remains, however, much smaller than the lasing frequency ω_Δ in all but the top contact layers.

We shall consequently approximate the Helmholtz equation for the lasing mode simply by

$$-\frac{\partial^2}{\partial x^2}E_0(x;z) - \frac{\omega^2}{c^2}n_r(x)^2E_0(x;z) = -q_{rad}(x)^2E_0(x;z) + \frac{\partial^2}{\partial z^2}E_0(x;z), \tag{38}$$

where we have also ignored the x-variation of q_{rad}. Finally, if we also assume a wide mesa (with extension in direction $\hat{z}$ larger than the modified wavelength, $\lambda/n_{mode} \equiv 2\pi/q_{rad}$) we arrive at the one-dimensional eigenvalue problem:

$$-\frac{\partial^2}{\partial x^2}E_0(x) - \frac{\omega^2}{c^2}n_r(x)^2E_0(x) = -q_{rad}^2E_0(x), \tag{39}$$

defined by the effective radiation-mode quantum-well confinement potential

$$\phi_\omega(x) = -n_r(x)^2\frac{\omega^2}{c^2}, \tag{40}$$

schematically illustrated in the lower panel of Figure 2.3.

The eigenvalues, $\varepsilon \equiv -q_{rad}^2$, of this potential problem defines the lasing mode which is confined within the waveguide core but does 'leak' through evanescent tails out into the waveguide cladding layers. The actual lasing mode wavevector q_{rad} is given by n_{mode} and the following effective potential barrier

$$\Delta\phi_\omega = \frac{\omega^2}{c^2}\left(n_{mode}^2 - n_{clad}^2\right) \tag{41}$$

determines the radiation decay in the waveguide cladding layers with index of refraction $n_{clad} \approx 3.15$. While this one-dimensional treatment is far from exact we use the Helmholtz equation in the cladding layers:

$$\frac{d^2}{dx^2} E_0 e^{\pm\kappa x/2} + \Delta\Phi_\omega \sim 0, \tag{42}$$

to provide an order of magnitude estimate of the radiation decay length

$$\begin{aligned} \frac{1}{\kappa} &\sim \frac{(c/\omega)}{\sqrt{n_{mode}^2 - n_{clad}^2}} \\ &= \frac{1}{2\pi} \frac{\lambda_\Delta}{\sqrt{n_{mode}^2 - n_{clad}^2}}. \end{aligned} \tag{43}$$

Using the reported Quantum Cascade Laser heterostructure parameters we find a decay length $1/\kappa \sim 0.4$ μm — significantly smaller than than the width of the waveguide cladding (~ 1 μm).

The above discussion is of course only schematic. However, it does illustrate the significant waveguide confinement, $\Phi = 0.46$, achieved in the quantum-cascade-laser design simply by including waveguide cladding layers with a lower average index of refraction.*

II.E The threshold optical characteristics

In Section II.C above we derived a formal estimate for the peak material gain, $\gamma_{mat} = gJ_{th}$. In the previous Section II.D we discussed the so-called waveguide-confinement factor, Φ, giving the fraction of the lasing mode intensity concentrated within the optically active superlattice. The peak threshold *effective* gain is thus $\Phi g J_{th}$. We conclude our discussion of the mid-infrared quantum cascade laser by a

* At the same time, however, it is also clear that such a waveguide confinement becomes increasingly more difficult for longer wavelengths. It may in particular be very difficult to achieve a good waveguide confinement in a hypothetical far-infrared quantum cascade laser. Such a discussion is beyond the scope of this dissertation.

comparison of the estimated peak material and effective gains with the estimated loss, α_I, and net emission rate, α_M, out from the end mirrors of the lasing cavity. The comparison in summarized in Table 2.4.

The design of a good waveguide confinement, i.e., a large value of Φ, using the variation of the index of refraction is an important element in the quantum-cascade-laser design. In Section II.C above we derived a formal estimate for the peak material gain, $\gamma_{mat} = gJ_{th}$. For the threshold current reported for the Ref. 1 (Ref. 3) cleaved mesa realization this estimate yield the threshold *material* gain $gJ_{th} = 99(155)\ \mathrm{cm}^{-1}$. Using the estimated value,[3] $\Phi \sim 0.5$, for the waveguide-confinement factor we predict a peak threshold effective gain of

$$\Phi g J_{th} \sim 45\ (78)\ \mathrm{cm}^{-1}, \tag{44}$$

directly proportional to Φ.

A good waveguide confinement (Φ) is also important in limiting the internal reabsorption α_I of the lasing mode. Specifically, the top contact layers and the InP substrate are heavily doped and has a plasmon energy comparable with the lasing frequency. However, the potentially dramatic plasmon reabsorption is avoided because only a vanishing part of the lasing mode intensity penetrate through the waveguide cladding layers.* As a consequence, the total internal loss is estimated at just $\alpha_I \approx 9\ (20)\ \mathrm{cm}^{-1}$ in Ref. 1 (Ref. 3.)

Summarizing the above results, the amplification of the lasing-mode intensity $S(y;\omega_\Delta)$ is at threshold described by a net gain

$$\frac{dS(y,\omega_\Delta)}{dy} = [\Phi g J_{th} - \alpha_I] > 0, \tag{45}$$

* The moderate doping concentration, $\leq 10^{18}\ \mathrm{cm}^{-3}$ of the cladding layers yields plasmon frequencies, $\omega_p \leq 43$ meV and causes no plasmon reabsorption.

TABLE 2.4 Threshold optical characteristics the quantum cascade laser realized both as a 12 μm $\times$ 0.72 mm cleaved mesa[1] (indicated by †) and as a 14 μm $\times$ 1.2 mm cleaved mesa[3] (indicated by ‡.) A simple two-level rate-equation description (see text) provides an estimate for the threshold density population inversion, Δn_{th}. Also listed are estimates for the optical transition matrix element, $\langle\Psi_4|x|\Psi_3\rangle \approx 10$ Å, between level E_4 and E_3. Such a large transition matrix element is possible because the quantum-confinement concentrates a very large oscillator strength, $f_{43} = 2m_e^*\Delta|\langle\Psi_4|x|\Psi_3\rangle|^2 \approx 0.4$, at the $E_4 \longrightarrow E_3$ optical transition. There is only a small spontaneous emission rate, $\bar{\Gamma}_{43}^{sp} = 5\times10^{-5}$ meV, at the mid-infrared frequency set by $\Delta = 295$ meV. However, the significant waveguide confinement factor, $\Phi \sim 0.5$, of the lasing mode intensity to the $N_p = 25$ optically active superlattice ensures a significant peak effective gain $\Phi g J_{th} \sim 45$–78 cm^{-1}. This value is larger than, but comparable to, the estimated total loss $\alpha_I + \alpha_M \sim 25$ cm^{-1} both due to the internal absorption, α_I, and due to the actual lasing emission rate, α_M, at the two end mirrors.

TABLE 2.4

Description:	*Symbol*	*Quantum Cascade Laser*$^{\dagger(\ddagger)}$
Subband separation (Lasing frequency)	Δ	$= 295$ meV
Optical matrix element‡	$\langle\Psi_4\vert x\vert\Psi_3\rangle$	≈ 10 Å
Spontaneous emission rate†	$\bar{\Gamma}_{43}^{sp}$	$\sim 5\times10^{-5}$ meV
Active period width $(L_{QB}+L_{Inj})$	—	$= 3.97\times10^{-2}$ μm
Total coupled active periods	N_p	$= 25$
Total width of active periods	—	≈ 1.0 μm
Width of wave-guide core	—	$= 1.68$ μm
Waveguide confinement factor$^{\dagger(\ddagger)}$	Φ	≈ 0.46 (0.5)
Internal loss$^{\dagger(\ddagger)}$	α_I	~ 9 (10) cm^{-1}
Threshold population inversion†	Δn_{th}	$\approx 1.7\times10^{11}$ cm^{-2}
Normalized gain coefficient$^{\dagger(\ddagger)}$	g	~ 9 (29) cm/kA
Peak threshold *material* gain$^{\dagger(\ddagger)}$	gJ_{th}	~ 99 (155) cm^{-1}
Peak effective threshold gain$^{\dagger(\ddagger)}$	ΦgJ_{th}	~ 45 (78) cm^{-1}
Length of cleaved mesa$^{\dagger(\ddagger)}$	L_{mesa}	$= 0.72$ (1.2) mm
Mirror reflection coefficient†	R_M	≈ 0.27
Mirror loss$^{\dagger(\ddagger)}$ $(-\ln(R_M)/L_{mesa})$	α_M	≈ 18.5 (11) cm^{-1}
Total loss	$\alpha_I+\alpha_M$	~ 28 (21) cm^{-1}

$^{\dagger(\ddagger)}$ Reported in Ref. 1 (Ref. 3).

because the significant waveguide-confinement factor, $\Phi \sim 0.5$, both increases the effective gain and limits the internal loss α_I.

However, to achieve threshold conditions, that is, the onset of *stimulated* emission and lasing, one must also ensure a containment in the in-plane direction of propagation of the lasing mode. Such a (longitudinal) containment is realized for the quantum cascade laser investigated in Ref. 1 (Ref. 3) by cleaving both ends of the 12 μm by 0.72 mm (14 μm by 1.2 mm) etched mesa structure.

The lasing threshold is characterized by a beginning build up of the radiation intensity inside the cavity formed by the cladding layers *and* by the two cleaved end mirrors. This concentration of the lasing mode is achieved when the net amplification during one passage of length L_{mesa} (from one end mirror to the other) exactly compensate for the intensity emitted at the first mirror. Denoting the reflection coefficient (of the lasing mode) at the end mirrors by R_M, the threshold condition becomes

$$R_M \exp\left([\Phi g J_{th} - \alpha_I] L_{mesa}\right) \equiv 1. \tag{46}$$

Introducing the so-called mirror loss,

$$\alpha_M \equiv -\ln(R_M)/L_{mesa}, \tag{47}$$

the above threshold condition, Eq. (46), can be reformulated simply as

$$\Phi g J_{th} = \alpha_I + \alpha_M. \tag{48}$$

That is, the lasing threshold obtains when the effective gain, $\Phi g J$, at current density J overcomes both the internal reabsorption and the mirror loss.

For the mesa structure reported on in Ref. 1 (Ref. 3,) we have $L_{mesa} = 0.72$ mm ($L_{mesa} = 1.2$ mm) and using the estimate,[1] $R_M = 0.27$, we obtain the estimate,

$\alpha_M = 18.5$ (11) cm^{-1}, for the mirror loss. The estimated total radiation loss, $\alpha_I + \alpha_M \approx 28$ (21) cm^{-1}, for the mesa structure investigated in Ref. 1 (Ref. 3) is thus smaller, but comparable to, the estimated peak effective gain, $\Phi g J_{th} =$ 45 (78) cm^{-1}.

We finally observe that α_M dominates the total radiation losses. It should thus be possible to achieve a significant reduction of the threshold current by changing the geometry of the lasing cavity. For example, increasing the mesa length L_{mesa} obviously reduces α_M, see Eq. (47), and in particular results in a larger peak optical power (see Table 2.3) for the longer quantum-cascade-laser-mesa realization (investigated in Ref. 3.) Furthermore, a significant improvement should be possible by increasing the effective reflection coefficient of the cavity mirrors. Such an improvement may in particular be achieved within a so-called quantum-disk-mesa realization[19,20] of a quantum cascade laser. In such quantum-disk lasers an effective potential for the radiation field confines also the in-plane extension of the lasing mode (in analogy with the confinement in the growth direction discussed in Section II.D.) This in-plane confinement potential causes the mirror loss to become extremely small because the lasing mode is not just reflected but must actually *tunnel* (through an effective potential barrier) out from the cavity.

REFERENCES

1. J. Faist, F. Capasso, D. L. Sivco, C. Sirtori, A. L Hutchinson, and A. Y. Cho, *Science* **264**, 553 (1994).

2. J. Faist, F. Capasso, D. L. Sivco, C. Sirtori, A. L. Hutchinson, and A. Y. Cho, *Electronics Letters* **30**, 865–866 (1994).

3. J. Faist, F. Capasso, D. L. Sivco, A. L. Hutchinson, C. Sirtori, S. N. G. Chu, and A. Cho, *Appl. Phys. Lett.* **65**, 2901 (1994).

4. C. Sirtori, F. Capasso, J. Faist, D. L. Sivco, A. L. Hutchinson, and A. Y. Cho, *Appl. Phys. Lett.* **66**, 4 (1995).

5. J. Faist, F. Capasso, C. Sirtori, D. L. Sivco, A. L. Hutchinson, and A. Cho, *Appl. Phys. Lett.* **66**, 538 (1995).

6. A. Imamoglu and R. J. Ram, *preprint*. This study details explains a possible quantum-cascade-laser-realization of inversionless lasing as discussed in for example A. Imamoglu and S. E. Harris, *Optics Letters* **Vol 14 No 24**, 1344 (1989).

7. Dr. F. Capasso, private communication; the author thanks Dr. Capasso for detailed discussions of the waveguide design during several phone conversations.

8. R. Ferreira and G. Bastard, *Phys. Rev. B* **40**, 1074 (1989).

9. A continuous-wave operation has been achieved in a later quantum-cascade-laser design; Dr. J. Faist, private communications.

10. Dr. F. Capasso, private communication.

11. G. P. Agrawal and N. K. Dutta, *Semiconductor Lasers,* (Van Nostrand Reinhold, N. Y., 1993,) pp. 1–24.

12. P. S. Zory, *Quantum Well Lasers,* (Academic Press, Inc., Boston, 1993.)

13. G. P. Agrawal and N. K. Dutta, *Semiconductor Lasers,* (Van Nostrand Reinhold, N. Y., 1993,) pp. 132–142.

14. A. Yariv, *Quantum Electronics* (John Wiley & Sons, Inc., New York, 1989), pp. 164–169.

15. J. N. Heyman, K. Craig, B. Galdrikian, M. S. Sherwin, K. Campman, P. F. Hopkins, S. Fafard, and A. C. Gossard, *Phys. Rev. Lett.* **72**, 2183 (1994).

16. J. N. Heyman, K. Unterrainer, K. Craig, B. Galdrikian, M. S. Sherwin, K. Campman, P. F. Hopkins, A. C. Gossard, To appear in *Phys. Rev. Lett.*.

17. G. P. Agrawal and N. K. Dutta, *Semiconductor Lasers,* (Van Nostrand Reinhold, N. Y., 1993,) pp. 25–73.

18. J. D. Jackson, *Classical Electrodynamics* (John Wiley & Sons, New York, 1962), pp. 339–346.

19. S. L. McCall, A. F. J. Levi, R. E. Slusher, S. J. Pearton, and R. S. Logan, *Appl. Phys. Lett.* **60**, 289 (1992).

20. A. F. J. Levi, R. E. Slusher, S. L. McCall, T. Tanbun-Ek, D. L. Coblentz, and S. J. Pearton, *Appl. Phys. Lett.* **60**, 289 (1992).